Improvement of temperature uniformity by using novel guide vanes in solar external receiver tubes

Yun Long [a,b,*], Zecan Tu [b,c], Daniela Piccioni Koch [b], Martin Frank [b], Rongsheng Zhu [a]

[a] National Research Center of Pumps, Jiangsu University, Zhenjiang 212013, China
[b] Steinbuch Centre for Computing, Karlsruhe Institute of Technology, Karlsruhe 76021, Germany
[c] College of Energy and Power Engineering, Nanjing University of Aeronautics and Astronautics, Nanjing 210016, China

Keywords:
Concentrated solar power
External receiver tube optimization
Guide vane
Molten salt
Heat transfer
Temperature uniformity

A B S T R A C T

The heat flux sustainability in solar external receiver tubes is limited by the non-uniformity of the temperature distribution and the maximum achievable temperature of the molten salt flow. In this paper, the external receiver tubes were equipped with novel guide vanes to enhance the heat transfer inside the tube and improve the uniformity of the temperature distribution on the tube surface. The geometric structures of guide vanes were optimized under non-uniform heat flux distributions. Firstly, the numerical models of tubes with different guide vanes (different wrap angles at trailing angle and different number of blades) were developed. Secondly, the numerical calculation of each case was carried out by using the fine meshing method, and was carried out by means of the commercial software ANSYS Fluent 19.2 on the High-Performance Computing. The SST k-ω turbulence model was used to predict the flow field inner the tube. The temperature, pressure loss, velocity and Nusselt number of these models predicted by CFD were analyzed and compared. Finally, the effect of different geometric parameters on the heat transfer enhancement and for improving the uniformity of temperature distribution were studied. It was observed that the guide vane is very effective to enhance the heat transfer inside the tube and improve the uniformity of temperature distribution on the tube surface. By optimizing the design of two parameters (wrap angles and number of blades), better heat transfer performance and improved uniformity can be obtained. For enhancing the heat transfer, and for improving the temperature uniformity and the flow resistance in the tube, a value of θ_{TE} 82° is should be chosen. With the increase of the blade number, the flow separation will be better controlled, and the swirling strength will increase gradually. To increase the number of blades helps to enhance the heat transfer and improve the temperature uniformity. A higher blade number will increase the system resistance and affect the thermal hydraulic performance, and increase the design head and power of the pump. The most convenient blade number is N 6. In addition, it was observed, that by adding the guide vanes, the flow resistance increases and this affects the thermo-hydraulic performance of the receiver tube. This study will provide theoretical basis and technical support for the efficient and reliable operation of solar collector heat exchanger tubes.

1. Introduction

Concentrated solar power (CSP) plants with thermal energy storage (TES) systems are regarded as very promising power sources in the future renewable energy system, since they can supply dispatchable and low-cost electricity with abundant yet intermittent solar energy [1]. Due to the large scale and electricity outputs, the solar power tower (SPT) system has received considerable attention [2]. A schematic view of a SPT power plant and some pictures of the demonstration facility Solar Two can be found in Fig. 1 [3].

The receiver is the key unit for the conversion of solar energy to thermal energy. In several SPT projects, the external receiver has been adopted, such as in the case of Solar Two [3] and SUPCON Delingha 50 MW [5]. Usually, the sunlight hits the receiver directly and cannot be concentrated on the full surface of the tube. As a consequence, the receiver tube is characterized by non-uniform solar flux distributions [6–7], which lead to thermal gradient on the receiver tube. This causes high thermal stress with consequent fractures [8], and thermal decomposition induced by local over-temperature of the heat transfer fluid [9]. The maximum value and uniform distributions of temperature on the tube wall and is also very important to keep the receiver work safely,

* Corresponding author at: National Research Center of Pumps, Jiangsu University, Zhenjiang 212013, China.
E-mail address: longyun@ujs.edu.cn (Y. Long).

Nomenclature

D	Diameter of the tube [mm]
f	Friction factor
h	Heat transfer coefficient [W/(m^2·K)]
L	Length [mm]
N	Blade number
Nu	Nusselt number
P	Pressure [Pa]
P_{in}	Pressure at the inlet [Pa]
P_{loss}	Pressure drop between inlet and outlet [Pa]
P_{out}	Pressure at the outlet [Pa]
q	Heat flux [kW/m^2]
Re	Reynolds number
S	Thickness [mm]
T	Temperature [K]
u	Velocity [m/s]
X, Y, Z	Global Cartesian coordinates

Greek symbols

β_{LE}	Blade angle at leading edge [°]
β_{TE}	Blade angle at trailing edge [°]
θ_{LE}	Wrap angle at leading edge [°]
θ_{TE}	Warp angle at trailing edge [°]
ρ	Density [kg/m^3]
λ	Thermal conductivity [W/(m·K)]
μ	Viscosity [kg/(m·s)]

Abbreviations

CSP	Concentrated Solar Power
SPT	Solar Power Tower
HTF	Heat Transfer Fluid
PEC	Performance Evaluation Criterion

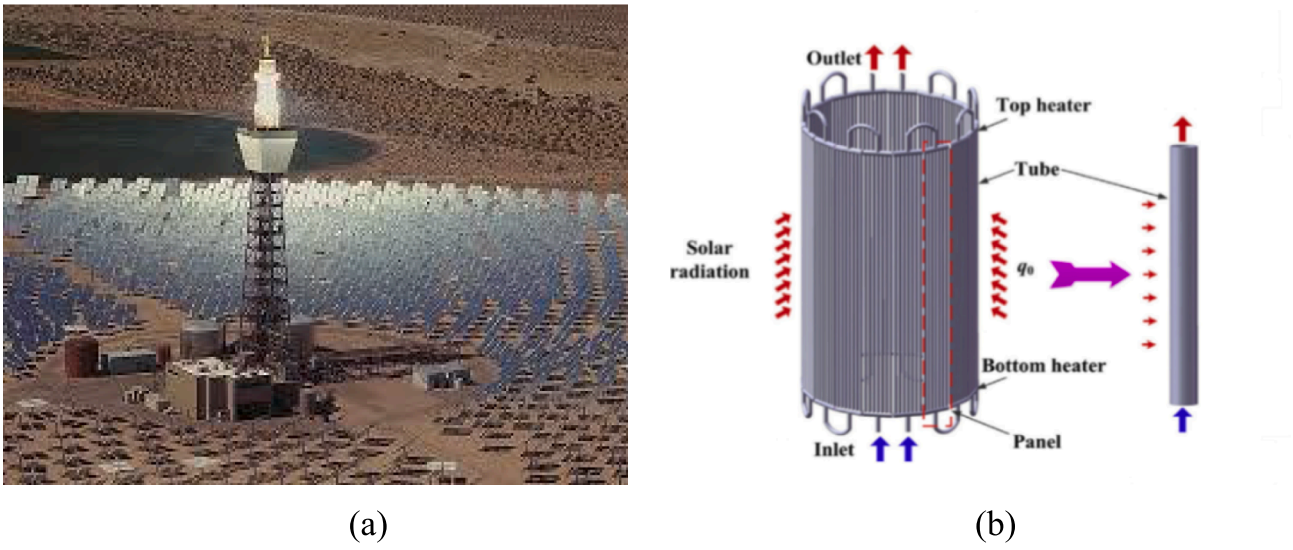

Fig. 1. (a) Schematic view of the SPT demonstration facility Solar Two [3] and (b) a solar external receiver tube [4].

which are commonly used in SPT external receivers [10]. The maximum operating temperature represents the relevant parameter of for solar power plants. The main limiting factors of their performances are the non-uniform distribution of temperature and the local high temperature in the receiver [11–13].

Many studies focused on the optimization of the solar flux distribution on the tube surface. These are based on the real-time optical model, on coupled models based on Monte Carlo Ray Tracing and on Finite Element Method, and different heliostat configuration strategies are also considered [14–17]. Sanchez-Gonzalez et al. [18] established a method to optimize the concentrated points of the heliostats in SPT systems and was able to achieve a peak heat flux reduction of 23% with slightly lower receiver interception. Gee et al. [19] and Wang et al. [20] added secondary reflectors near the receiver tube to reflect sun light to the back side of the receiver and worked out a more uniform solar flux distribution. However, in the case of SPT external receivers, it is very challenging to flatten the solar flux distribution on the entire surface of the tube, due to its particular geometric structure and light tracing methods.

Another solution for optimizing the uniformity of the temperature distribution is to increase the transverse mixing to enhance the heat convection on the inner tube wall. The enhancement in heat transfer convection inside a tube has been investigated and tested in the design of tubular heat exchangers [21–22]. Munoz et al. [23] studied the effects of the number of fins and the helix angle on the heat convection enhancement of the internally helically finned tubes and could improve the collector efficiency by a factor of about 3% compared to that of a smooth tube. Cheng et al. [24] adopted a method to improve heat convection enhancement by placing the vortex generators inside the wall of parabolic trough tubes. Borunda et al. [25] analyzed and optimized the performance of a parabolic trough collector with a twisted-tape insert, and demonstrated that the twisted-tape insert could reduce the peak temperature of the tube and also achieves good collector efficiencies.

In order to improve the uniformity of temperature and the heat transfer performance, our team also do some research. Zecan Tu et al. [26] built models of the smooth tube and the tube with guide vanes to investigate the heat transfer enhancement and the mixing effect due to guide vanes. The distributions of the temperature, velocity, turbulence intensity, and *Nu* predicted by these two models were compared. The results showed that the guide vanes form swirling flows, reduce the maximum tube and molten salt temperatures, and improve the heat transfer. The effects of different guide vane blade shapes on heat transfer

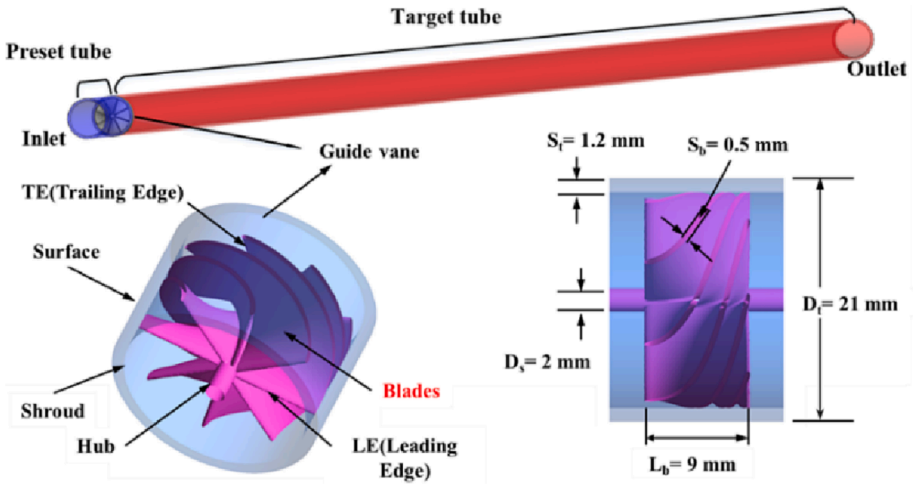

Fig. 2. Schematic of the receiver tube with guide vanes.

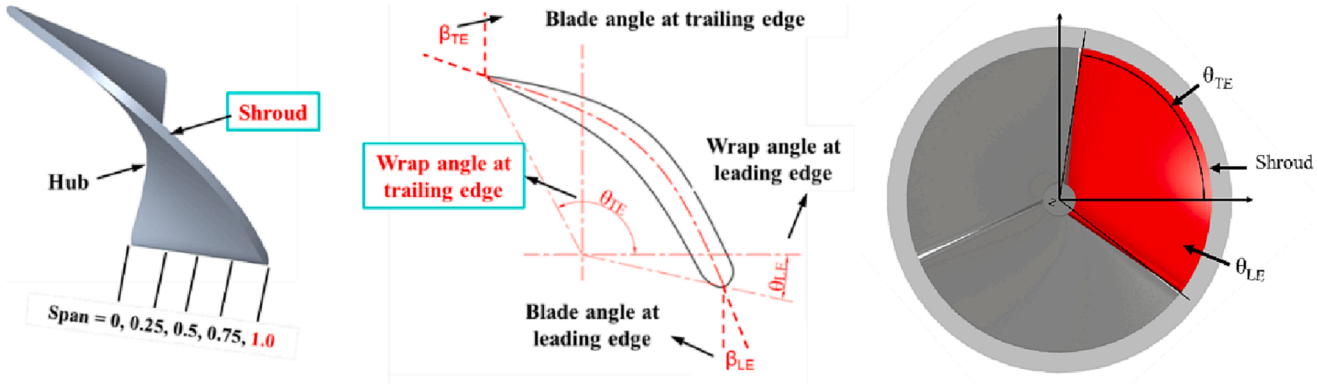

Fig. 3. Definition of the blade.

and pipe resistance were not investigated. Mahfuja Khuda et al. [27] carried out a numerical analysis of developing flow and conjugate heat transfer in a solar receiver tube with a three-blade guide vane at the tube inlet, and investigate the effect of guide vane and working fluid on the flow and temperature distribution in a solar receiver tube subjected to the boundary condition of the non-uniform wall heat flux. Wang Dezhong et al. [28–30] improved the swirl strength in the tube by adding a guide vane separator, promoted the aggregation of bubbles in the tube, and realized the removal of gas by forming a spiral gas column.

In this analysis, the external receiver tube was equipped with novel guide vanes to enhance the heat transfer inside the tube and improve the uniformity of the temperature distribution on the tube surface. This was numerically studied by considering non-uniform heat flux distributions. Firstly, the numerical models of tube with different guide vanes (different wrap angles at trailing angle and blade numbers) were created. Then, the temperatures, pressure losses, velocities and Nusselt numbers predicted by these models were analyzed and compared, to study the heat transfer enhancement and the mixing effect of guide vanes. Finally, the effect of different geometric parameters on the heat transfer enhancement and the flow mixing were studied. This study will provide theoretical basis and technical support for the efficient and reliable operation of solar collector heat exchanger tubes.

2. Technical approach

2.1. Numerical models

The numerical models in this simulation are based on the typical tube of the external receiver of Solar Two [3], where the height of the whole receiver is 6200 mm. A single tube with an additional guide vane in the receiver was considered for building the numerical model (Fig. 2). The computational domain consists of three parts: the preset tube, the guide vane and the target tube. The preset tube is used to achieve a fully developed flow before the vanes. The length of the preset tube L is 200 mm. The length of the downstream target tube is 6000 mm. The length of guide vane is 9 mm. Concerning the cross section of the tube, the outside diameter D_t of the tube is 21 mm, and the thickness S_t of the tube wall is 1.2 mm. The geometry of the guide vanes is shown in Fig. 2. The number of vanes is 8. The length in the axial direction L_b and the thickness of the blade S_b are 9 mm and 0.5 mm, respectively. The guide vanes are connected by a cylinder with a 2 mm diameter.

The blade is defined as shown in Fig. 3 and is divided into five layers of profiles (Span = 0, 0.25, 0.5, 0.75, 1.0) from the hub to the shroud. The profile of each layer is controlled by the warp angle at leading edge θ_{LE}, wrap angle at trailing edge θ_{TE}, blade angle at leading edge β_{LE}, blade angle at trailing edge β_{TE}.

2.2. Governing equations

The steady state simulations were carried out by means of the commercial software ANSYS Fluent 19.2 [31] on the High-Performance Computing (HPC) systems of Baden-Württemberg in Germany [32]. The continuity, momentum and energy governing equations are [33]:

$$\frac{\partial \rho \overline{u_i}}{\partial x_i} = 0 \tag{1}$$

Table 1
Boundary conditions [26].

Domain	Parameter	Value
Fluid	Temperature at inlet	563 K
	Mass flow rate at inlet	1.4 kg/s
	Turbulence intensity at inlet	5%
	Pressure at outlet	1 atm
Solid	Peak heat flux q_{max} on the tube outer surface	800 kW/m^2

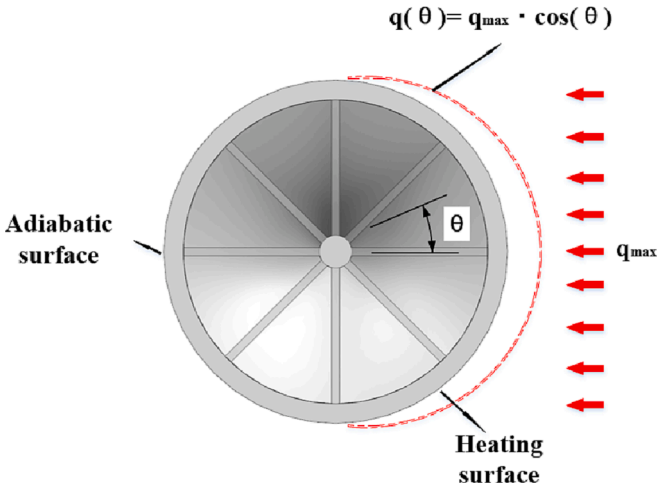

Fig. 4. Distribution of the heat flux on the tube surface [26].

$$\rho\overline{u}_j\frac{\partial\overline{u}_i}{\partial x_j}=\rho\overline{F}_i\quad\frac{\partial\overline{p}}{\partial x_i}+\frac{\partial}{\partial x_j}\left[\mu\left(\frac{\partial\overline{u}_i}{\partial x_j}+\frac{\partial\overline{u}_j}{\partial x_i}\right)\quad\rho\overline{u_i'u_j'}\right] \tag{2}$$

$$\rho\overline{u}_j\frac{\partial\overline{T}}{\partial x_j}=\frac{\partial}{\partial x_j}\left(\frac{\lambda}{c_p}\frac{\partial\overline{T}}{\partial x_j}\quad\rho\overline{u_j'T'}\right) \tag{3}$$

where ρ, μ, λ and c_p are the density, viscosity, thermal conductivity, and specific heat capacity of the molten salt, respectively. $\overline{F}_i$ is the body force, where the over-line denotes the average value. The term $\rho\overline{u_i'u_j'}$ represents the Reynolds stress tensor and $\rho\overline{u_j'T'}$ expresses the turbulent heat flux.

According to A. Fritsch's previous studies [34], the k-ω turbulence model proved to be suitable for the simulation of the heat and mass transfer in the tube flow. The transport equations for the turbulent kinetic energy (k) and its specific dissipation rate (ω) are expressed as [31]:

$$\frac{\partial}{\partial x_i}(\rho k u_i)=\frac{\partial}{\partial x_j}\left[\Gamma_k\frac{\partial k}{\partial x_j}\right]+G_k\quad Y_k+S_k+G_b \tag{4}$$

$$\frac{\partial}{\partial x_i}(\rho\omega u_i)=\frac{\partial}{\partial x_j}\left[\Gamma_\omega\frac{\partial\omega}{\partial x_j}\right]+G_\omega\quad Y_\omega+S_\omega+G_{\omega b} \tag{5}$$

where G_k and G_ω are the generation of turbulence kinetic energy and ω. Γ_k and Γ_ω represent the effective diffusivity of k and ω, while Y_k and Y_ω represent the dissipation of k and ω due to the turbulence. S_k and S_ω are user-defined source terms, while G_b and $G_{\omega b}$ represent the buoyancy terms.

For the tube and the guide vanes, which are the solid region of computational domain, the energy transport equation under steady conditions is [31]:

$$\nabla\cdot(\vec{v}\rho h)=\nabla\cdot(\lambda\nabla T)+S_h \tag{6}$$

where h is the sensible enthalpy, λ is the thermal conductivity, and S_h is the volumetric heat source.

Table 2
Thermal properties of the molten salt and stainless steel [26].

Parameter		Value
Molten salt (fluid medium)	Density (kg/m^3)	2090–0.636·(T-273.15)
	Heat capacity (J/(kg·K))	1443 + 0.172·(T-273.15)
	Heat conductivity (W/(m·K))	0.443 + 1.9·10^{-4}·(T-273.15)
	Viscosity (kg/(m·s))	0.022714–1.2·10^{-4}·(T-273.15) + 2.281·10^{-7}·(T-273.15)^2-1.474·10^{-10}·(T-273.15)^3
Stainless steel (solid tube material)	Density (kg/m^3)	8000
	Heat capacity (J/(kg·K))	500
	Heat conductivity (W/(m·K))	21.5

For the solution method, the simple coupling method between pressure and velocity was adopted. The second order for pressure, the second order upwind for the momentum and energy, and the first order upwind for the turbulent kinetic energy were considered in this simulation [26].

2.3. Boundary conditions

The computation domains here considered include the fluid and the solid domain. The boundary conditions are summarized in Table 1. In order to simulate the non-uniformity of the solar flux on the tube wall, a cosine radial distribution of the heat flux is considered on the half surface of the tube wall (X ≥ 0), q(θ) = q_{max}·cos(θ), which is referred to as heating surface. The distribution of the heat flux on the tube surface is shown in Fig. 4. On the other half surface (X < 0), the adiabatic wall condition is applied and this is indicated as adiabatic surface [26]. In the axial direction, the distribution of heat flux is kept constant. The boundary conditions applied are summarized in Table 1 [26].

The tube is made of stainless steel and is filled with molten salt (Solar Salt, 60% by weight $NaNO_3$ and 40% by weight KNO_3) [26]. The thermal properties of molten salt and stainless steel [10] are given in Table 2, where the temperature T is given in Kelvin.

2.4. Parameter definitions

In order to demonstrate the results, a specific outside surface of the target tube S1 (0 m < Z < 1 m) and a cross section S2 (Z = 0.25 m) were defined. In addition, the following specific lines are introduced: Line 1 (yellow color) on the outside tube surface where heat flux reaches the peak value (X = 0.021 m, Y = 0 m, 0 m < Z < 6 m), and Line 2 (blue color) on the inside tube wall, with closest position to peak heat flux (X = 0.0186 m, Y = 0 m, 0 m < Z < 6 m). The geometry of surfaces S1 and S2 and Lines 1 and 2 is shown in Fig. 5.

According to previous studies [24], the Reynolds number Re is used to represent the flow state, and the Nusselt number Nu is used to represent the heat convection performance on the inside wall of the tube. Re and Nu are defined by Eqns. (7) and (8):

$$Re=\frac{\rho uD}{\mu} \tag{7}$$

$$Nu=\frac{hD}{\lambda_f} \tag{8}$$

where u, ρ and μ are the velocity, density and viscosity of the molten salt flow at the inlet, D represents the inside diameter of the tube, h is the heat transfer coefficient on the inside wall of the tube and λ_f is the thermal conductivity of the molten salt. The peripherally averaged Nu is the average value of the Nu on the circle line with constant Z.

The temperature difference ΔT between the maximum and minimum temperature on the tube cross section is given as [26]:

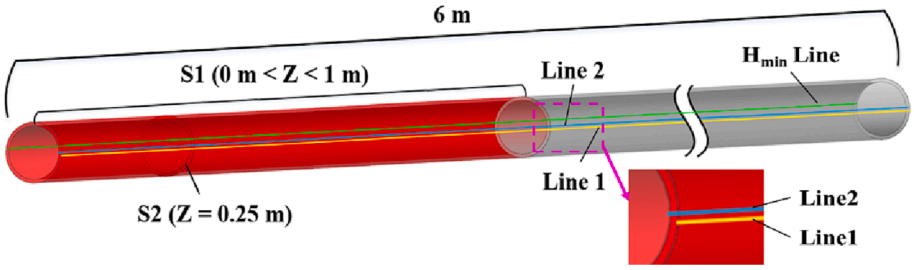

Fig. 5. Schematic diagram of the specific faces and the lines on the target tube.

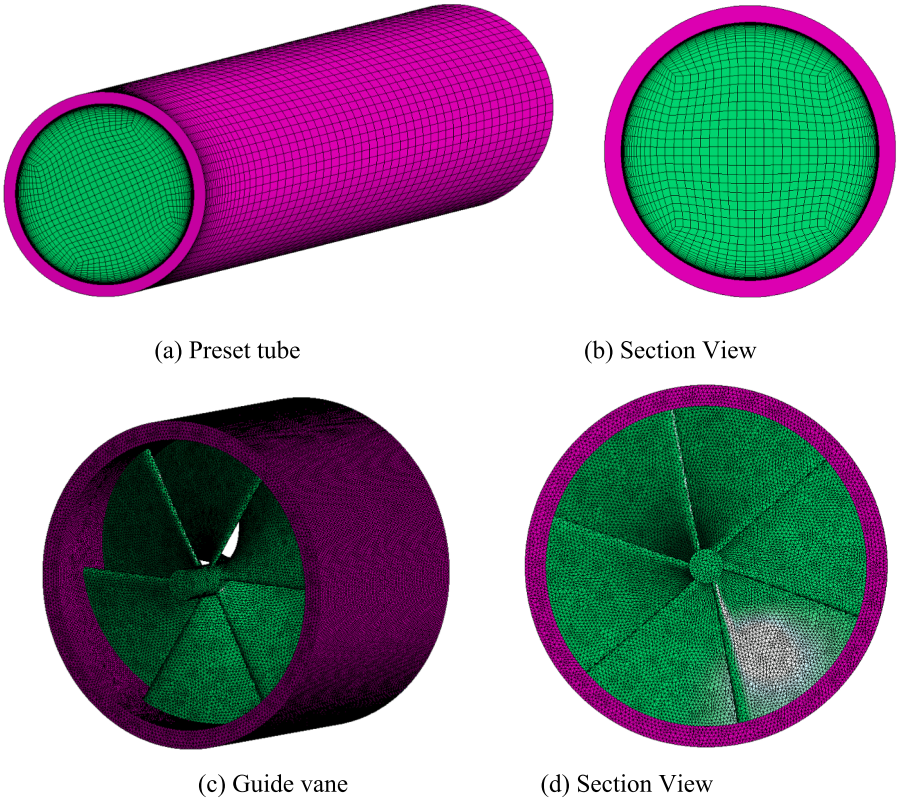

Fig. 6. Schematic diagram of the numerical grid.

$$\Delta T = T_{\max} \quad T_{\min} \tag{9}$$

The pressure drop P_{loss} between the pressure P_{in} at the inlet of the guide vane component and the pressure P_{out} at the outlet of the tube is used to represent the pressure loss [26].

$$P_{loss} = P_{in} \quad P_{out} \tag{10}$$

The friction factor f is defined as [35]

$$f = \frac{P_{loss}}{L}\frac{D}{(1/2)\rho u^2} \tag{11}$$

Where P_{loss} is the differential pressure between the inlet and outlet of enhanced receiver tube, f is used to evaluate the pressure drop when the enhancement techniques are adopted to increase heat transfer.

The performance evaluation criterion (PEC) of heat transfer enhancement Nu/Nu_{c} under constant pressure drop f/f_c is given by [4]

$$\text{PEC} = \frac{Nu/Nu_c}{(f/f_c)^{1/3}} \tag{12}$$

where the subscript "c" represents clear or smooth receiver tube, which like the target tube in Fig. 2, without guide vane or no other parts just the tube. It is often required that based on such data heat transfer performance comparisons can be examined. When PEC is more than 1, it represents better thermal hydraulics, and when PEC is<1, flow resistance will increase, representing poor thermal hydraulics.

2.5. Mesh

The meshing here considered, consists of a combination of structured and unstructured meshes. The preset tube and the target tube use structured hexahedral grids. For the guide vanes, the unstructured tetrahedral grid is adopted, due to the more complex structure, which is required to analyze this part of the device. The effect of the number of grid points on the temperature distribution on the tube surface were studied [26]. The results showed that when the number of grid points equals 5806037, the average relative variation of the temperature is smaller than 1%, if the number of grid points continues to increase, and the temperature keeps constant. Therefore, the discretization grid with more than 5,806,037 elements was adopted in the simulation. This is shown in Fig. 6. The number of grids for the target tube, for the solid component with guide vane, for the fluid component with guide vane and for the preset tube are 4648597, 1680794, 1,161,695 and 188917,

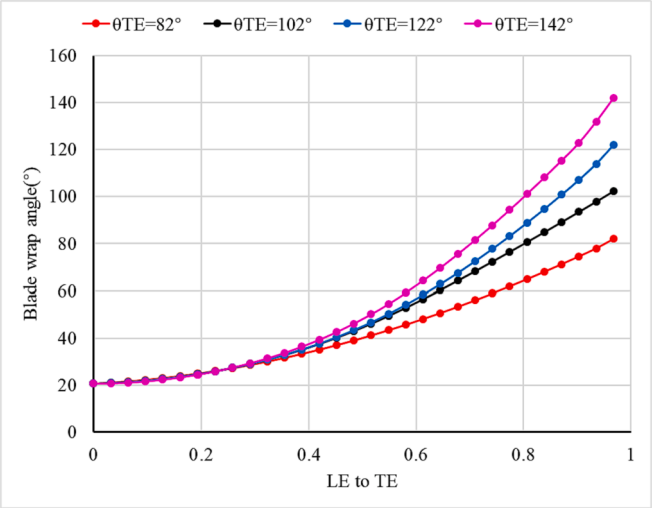

Fig. 7. Wrap angle distribution of different blade trailing angle cases.

respectively.

2.6. Optimization cases

There are many parameters of the guide vane blades that affect the heat transfer enhancement. This study focuses on two cases:

Case 1: Optimization of θ_{TE} (Wrap angle at trailing edge) at Shroud and.
Case 2: Optimization of N (Number of blades).

For Case 1, θ_{TE} is 82°, 102°, 122°, 142°. For the guide vane design, the wrapping angle and outlet angle are the main control parameters for generating the swirl component and increasing the swirl strength. In order to obtain the effect of different wrap angles on the heat transfer effect and the uniformity improving, set a wrap angle every 20°. The purpose of this paper is to obtain the influence of multi-parameter variables on swirl by changing multiple parameters (wrap angle and blade number) of guide vane geometry, and then obtain the influence of multi-parameter variables on heat transfer by changing the swirl intensity. Among them, select the wrap angle to cover a certain range. The start and end values of the blade wrap angle are mainly determined according to the distribution of the blade flow channel. It not only considers that the flow channel is too narrow due to increasing the wrap angle, resulting in too fast flow velocity in the flow channel, and avoids the small swirl velocity caused by too small the wrap angle..

For different θ_{TE}, the wrap angle distributions along the shroud section from leading edge to trailing edge are shown in Fig. 7. Based on the θ_{LE} and θ_{TE}, the spline curve is used for smooth fitting to determine the distribution law of each case. All θ_{LE} are designed to 20°, and the wrap angle changes slowly near the leading edge to ensure that the blade angle at leading edge approach 0°. Geometry of different wrap angles at trailing angle are shown in Fig. 8. The blade to blade profile is at the shroud of the blade. Although the blade is controlled by five layers of profiles, as shown in Fig. 3, the control of all profiles is associated in the design, so that only the shroud profile can be controlled to design the entire blade shape.

For Case1, N are respectively designed to 3, 4, 5, 6, 7, 8. Fig. 9 shows the geometry of different blade number cases. Optimization cases are based on $\theta_{TE} = 142°$.

This research mainly focuses on the heat transfer in the tube with non-uniform heat-flux. Nmerical analysis of heat transfer in the tube with different guide vane (different wrap angle at trailing edge and blade number) for molten salt was carried out.

3. Results and analysis

3.1. Effects on heat transfer characteristics for different wrap angles at trailing edge

The guide vane enhances the heat transfer convection in the receiver

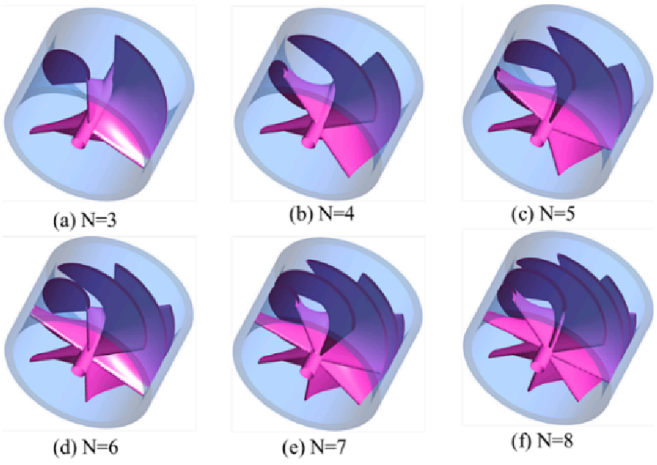

Fig. 9. Geometry of different blade numbers.

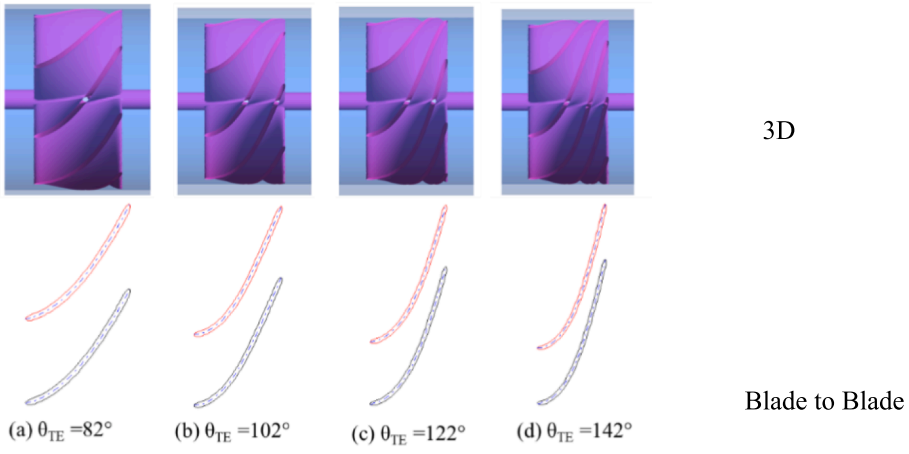

Fig. 8. Geometry of different wrap angles at trailing angle.

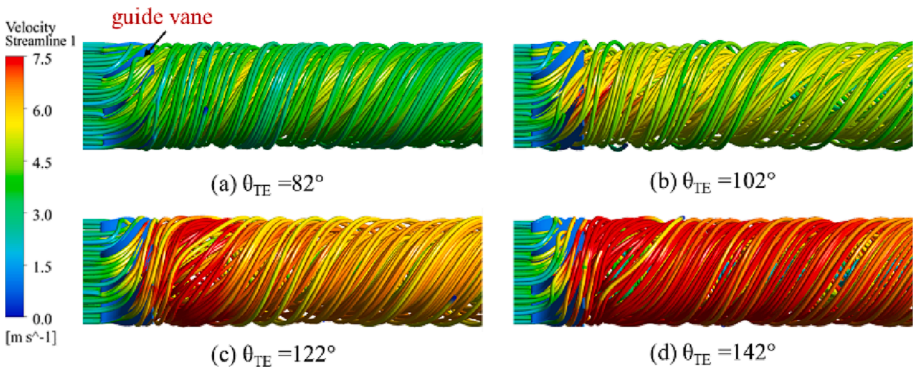

Fig. 10. Velocity streamline behind the guide vane for different θ_{TE}.

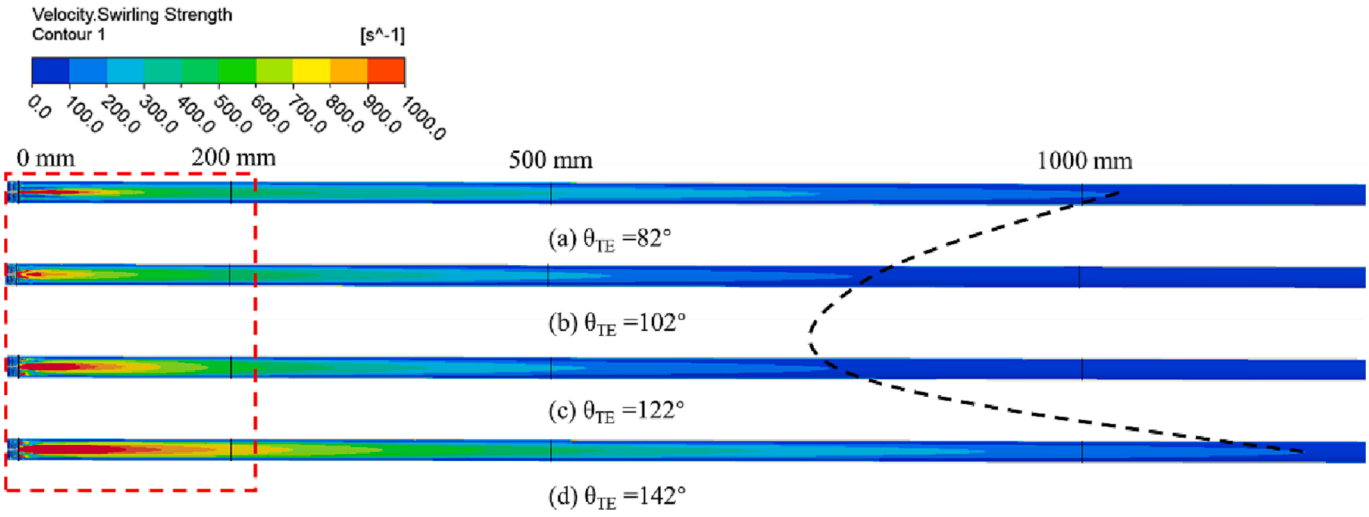

Fig. 11. Velocity swirling strength distribution for different θ_{TE} angles.

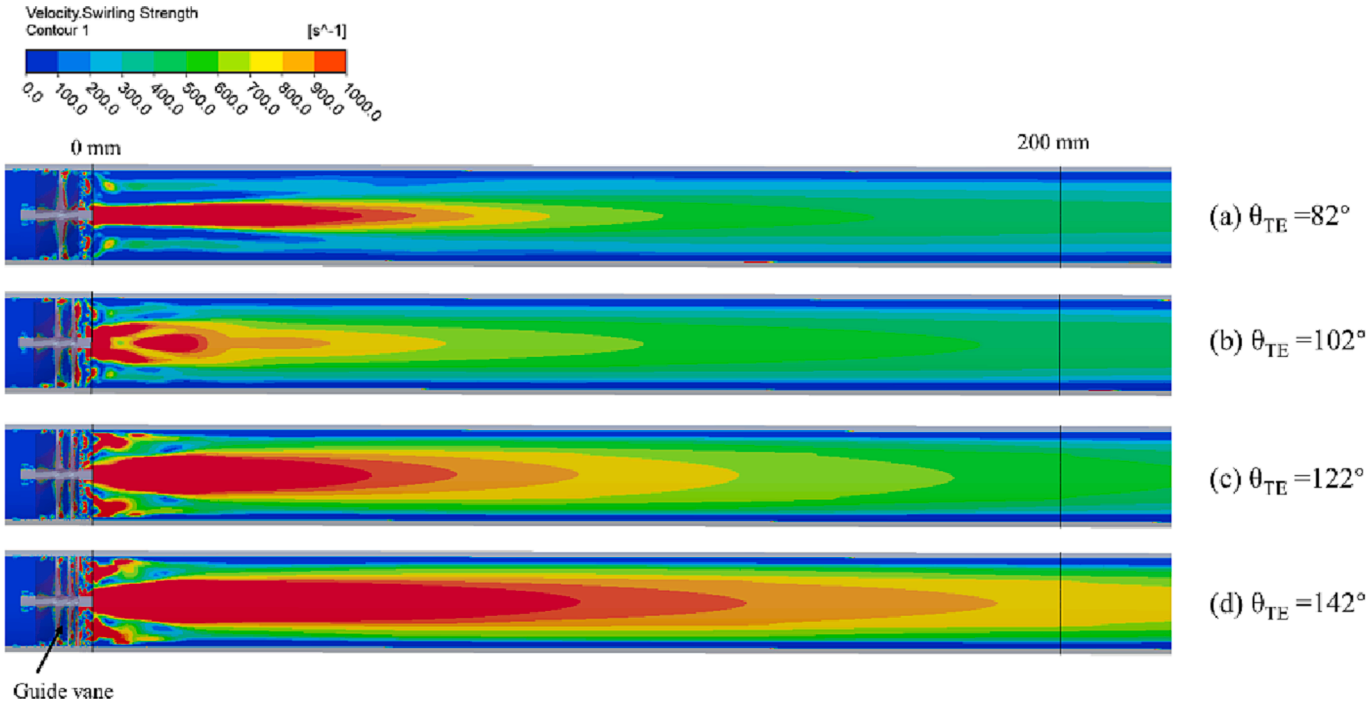

Fig. 12. Velocity swirling strength distribution (from 0 to 200 mm) for different θ_{TE} angles.

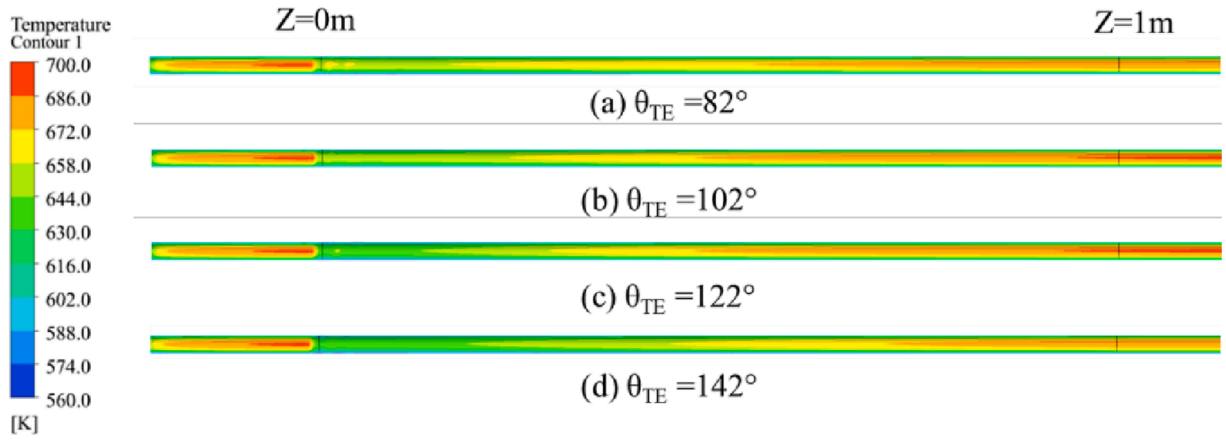

Fig. 13. Temperature contours on S1 for different θ_{TE} angles.

tube mainly by rebuilding the velocity field in it. Fig. 10 shows the velocity streamline behind the guide vane for different θ_{TE}. As θ_{TE} increases, the flow velocity in the tube behind the guide vane is faster and it can be concluded that the convective heat transfer can be enhanced by guide vanes. It can be seen from the Fig. 8 that with the increase of the blade wrap angle θ_{TE}, the flow channel between the blades becomes narrower and narrower, which will increase the fluid velocity at the outlet of guide vane. At the same time, flow velocity in the target tube also increases significantly for increasing θ_{TE}. Usually, this velocity grow includes two directions, one is the circumferential direction and the other is the axial direction, wherein the circumferential direction speed will increase the swirl intensity to better improve the heat transfer of the tube inner wall. Higher circumferential velocity means that the fluid will acquire higher vortex strength after flowing out of the guide vane, resulting in larger heat transfer capacity.

In order to further explain the influence of different guide vane θ_{TE} on the inner flow in the target tube, we select the velocity swirling strength inside the guide vane and target tube to compare the differences of the different schemes, as show in Fig. 11. Here, the length of the lower boundary of the velocity swirling strength scale 100–200 s^{-1} is used to evaluate the swirling strength and the ability to enhance heat transfer of different guide vane schemes. The length of the target tube is 6000 mm, but only the length range near 0–1000 mm for comparison in Fig. 11 is considered, since after more than 1000 mm, the difference in swirling strength is small. It can be observed that, the lower boundary 100 s^{-1} does not vary linearly with the wrap angle θ_{TE}, as shown by the black dotted line in Fig. 11. The length of $\theta_{TE} = 142°$ is much higher than 1000 mm, the length of $\theta_{TE} = 82°$ is near 1000 mm, and the length of $\theta_{TE} = 102°$ and $\theta_{TE} = 122°$ are much lower than the others.

In order to further reveal the influence mechanism of the guide vane on the swirling, we select the swirling strength distribution within 0–200 mm, as shown in Fig. 12. In the case $\theta_{TE} = 82°$, the larger swirling strength at the tail of the guide vane is mainly concentrated in the middle part. In the case $\theta_{TE} = 102°$, the distribution of swirling strength starts to change. The influence of guide vane parameters on the swirling strength in the long tube begins to show regularity, that is, the swirl intensity spreads from the middle of the tube to gradually increase and spread to the tube wall. The other three basic distributions are consistent. It is obvious that the strength of the case $\theta_{TE} = 142°$is greater than the case$\theta_{TE} = 82°$, $\theta_{TE} = 102°$ and $\theta_{TE} = 122°$. The length of the lower boundary 100 s^{-1} of the case $\theta_{TE} = 142°$ is much larger than the other three cases.

Fig. 13 shows temperature contours on the outer surface of receiver tube S1 for different wrap angles at trailing edge θ_{TE}. In order to evaluate the effects of different θ_{TE} angles on the temperature uniformity, the preset tube, guide vane, and target tube with 0 m < Z < 1 m were selected. In comparison to the temperature distribution on the smooth tube [26], it is evident that the temperature field on the receiver tube can be significantly rebuilt by guide vane. In Fig. 13, it can be observed that on the preset tube, the wall with high heat flux density corresponds to a higher temperature, and there is an expected temperature gradient. The temperature on tube surface drops significantly, especially for $\theta_{TE} = 82°$ and $\theta_{TE} = 142°$. The temperature on tube surface for $\theta_{TE} = 102°$ and $\theta_{TE} = 122°$ has little differences. After the guide vane, the temperature of the high heat flux wall surface decreases significantly. This indicates that the guide vane is very effective in enhancing the heat transfer inside the tube and can improve the temperature uniformity distribution on the tube surface. With the weakening of the swirling flow in the tube, the heat transfer gradually decreases, and the temperature of the high heat flux surface increases accordingly along the axial direction. Despite this, on the target tube, the temperature efficiently decreases in the range 0 m < Z < 1 m, leading to a reduction of the thermal stress caused by high temperature gradients.

Fig. 14 shows the temperature distributions on Line 1 for different θ_{TE} values. As mentioned before, Line 1 is on the outside tube surface where the heat flux reaches its peak value (at X = 0.021 m, Y = 0 m, 0 m < Z < 6 m). Fig. 14 (a) shows the temperature distributions on Line 1 from 0 m < Z < 6 m. Compared with the smooth tube [26], it is observed that after adding the guide vane, the temperature on Line 1 is significantly reduced. For a smooth tube, the temperature of Line 1 increases gradually along the axial direction, almost linearly. For the tube with guide vanes, the temperature on Line 1, for different θ_{TE} angles, decreases rapidly at the beginning along the axial direction, mainly because the guide vane swirl has a considerable effect on enhancing the heat transfer. With the weakening of the swirling flow in the tube, the heat transfer gradually decreases. After Z = 3 m, the temperature on Line 1 for different θ_{TE} angle varies slightly. The overall temperature distribution on Line 1 for each θ_{TE} is about 50 K lower than that of the smooth tube, which effectively reduces the thermal stress caused by the high temperature gradient on the tube wall. In order to better evaluate the effects of different wrap angles on the temperature, two different tube areas were considered: 0 m < Z < 1 m and 2 m < Z < 3 m), as shown in Fig. 14 (b) and Fig. 14 (c).

As shown in Fig. 14 (b), for different θ_{TE} angles, different temperature distributions are observed. Moreover, in the axial direction, the temperature does not quite decrease for increasing θ_{TE} value. In particular, for 0 < Z < 0.3, the temperature decreases in the axial direction when the wrap angle θ_{TE} increases. In Fig. 14(b), it can be observed that for Z greater than 0.4, the temperature does not decrease for increasing wrap angle θ_{TE}. For $\theta_{TE} = 142°$ a first impact on the temperature of Line 1 is observed. For $\theta_{TE} = 82°$, a second effect on the temperature of Line 1 for Z greater than 0.4 is observed. The temperature curves for $\theta_{TE} = 102°$ and $\theta_{TE} = 122°$ become closer for Z greater than 0.4. This situation is maintained along the axial direction, as shown

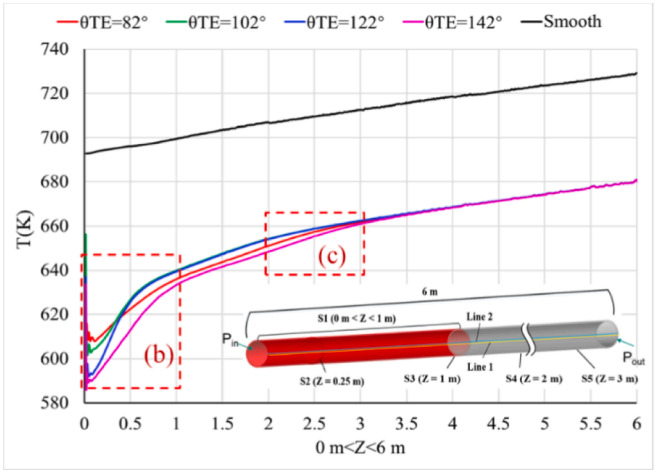

(a) 0 m< Z <6 m

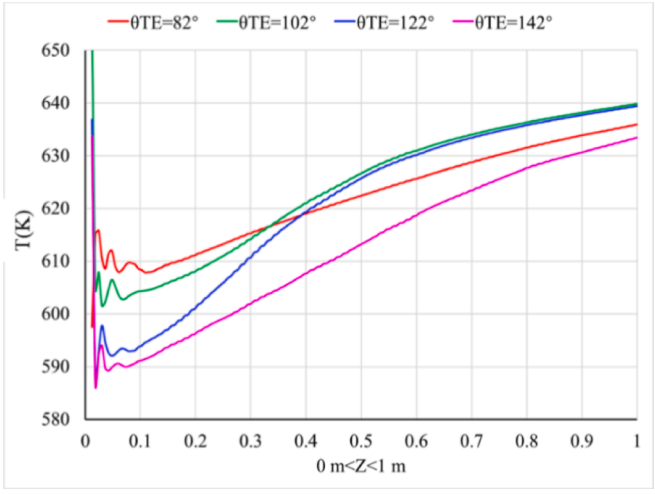

(b) 0 m< Z <1 m

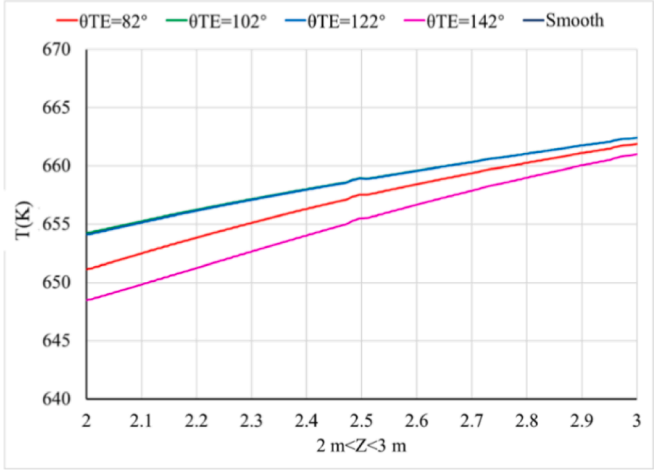

(c) 2 m< Z <3 m

Fig. 14. Temperature distributions on Line 1 for different θ_{TE} angles.

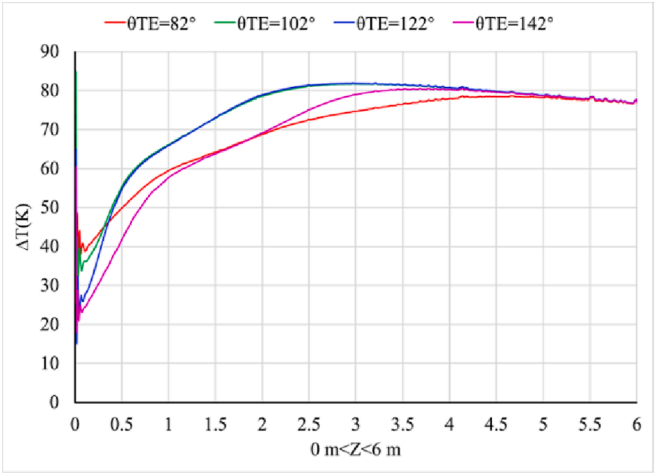

Fig. 15. Temperature difference ΔT between Line 1 and H_{min} Line for different θ_{TE} angles.

in Fig. 14(c). The case of $\theta_{TE} = 142°$ have a larger impact on temperature of Line 1 from 2 m to 3 m. From the results of enhanced heat transfer, the heat transfer effect of each case is consistent with the swirling strength distributions (the length of the lower boundary of the velocity swirling strength scale 100–200 s^{-1}) in Fig. 11. The swirling plays a major role in enhancing the heat transfer.

Fig. 15 shows the temperature difference between Line 1 and H_{min} Line for different θ_{TE} angles. The temperature curves for $\theta_{TE} = 102°$ and $\theta_{TE} = 122°$ get closer along the full tube. For $\theta_{TE} = 82°$ and $\theta_{TE} = 142°$, both have larger impact on H_{min} Line. From the perspective of improving temperature uniformity, the case of $\theta_{TE} = 82°$ and $\theta_{TE} = 142°$ are better. Temperature difference of the case $\theta_{TE} = 142°$ is lower than other cases from 0 m to 1.5 m. Temperature difference of the case $\theta_{TE} = 82°$ is lower than other cases from 2 m to 6 m.

Table 3 shows key performances with different angle θ_{TE} angles. The key performances include the Nusselt number *Nu*, the pressure drop P_{loss}, the friction factor *f*, the performance evaluation criterion (PEC), which are defined in Equation (7)–(12).

According to the data in the Table 3, the variation laws of four key performances (Nusselt number *Nu*, Pressure loss P_{loss}, *f* and PEC) with θ_{TE} are analyzed respectively, as shown in Fig. 16. From Fig. 16(a), it can be observed that *Nu* first decreases and then increases along the axial direction. This means case $\theta_{TE} = 82°$and case $\theta_{TE} = 142°$ can enhance the convection heat transfer better, same with the analysis of Figs. 11-15. From Fig. 16(b), it can be noticed that P_{loss} increases with increasing θ_{TE}. It can be seen from Fig. 16 (d) that the PEC value gradually decreases with the increase of θ_{TE}. Therefore, a growth of the θ_{TE} angle can enhance the convection heat transfer, with a consequent pressure loss and pump power grow. Therefore, it is necessary to discuss heat transfer enhancement and hydraulic performance integrally. Fig. 16(d) shows that the values of PEC are lower than 1.0, which means that the thermo-hydraulic performance is poor. Although adopting guide vanes can enhance heat exchange, this also will increase the system resistance and affect the thermal hydraulic performance. It is necessary to increase the design head and power of the pump, which will increase the cost of equipment and project costs. Considering the above factors, case $\theta_{TE} = 82°$ is better.

Fig. 17 shows *Nu* distributions on Line 2 for different θ_{TE}. As mention before, Line 2 is on the inside tube wall, with closest position to peak heat flux (X = 0.0186 m, Y = 0 m, 0 m < Z < 6 m). Fig. 17 (a) shows the *Nu* distributions on Line 2 from 0 m < Z < 6 m. Compared with the smooth tube [26], it is clear that after adding the guide vane, the *Nu* distributions on Line 2 is larger at the beginning (0 < Z < 1 m), mainly because the guide vane swirling has a great effect on enhancing heat transfer. However, *Nu* distributions on Line 2 become lower than smooth

Table 3
Key performances with different θ_{TE}.

θ_{TE}	Nu	P_{loss}	f	Nu_c	P_{lossc}	f_c	PEC
82°	28.381	61783.9	0.02112	29.308	46373.1	0.01579	0.40474
102°	28.128	72064.0	0.02464	29.308	46373.1	0.01579	0.25279
122°	28.131	106815.0	0.03652	29.308	46373.1	0.01579	0.07764
142°	28.344	131964.0	0.04512	29.308	46373.1	0.01579	0.04148

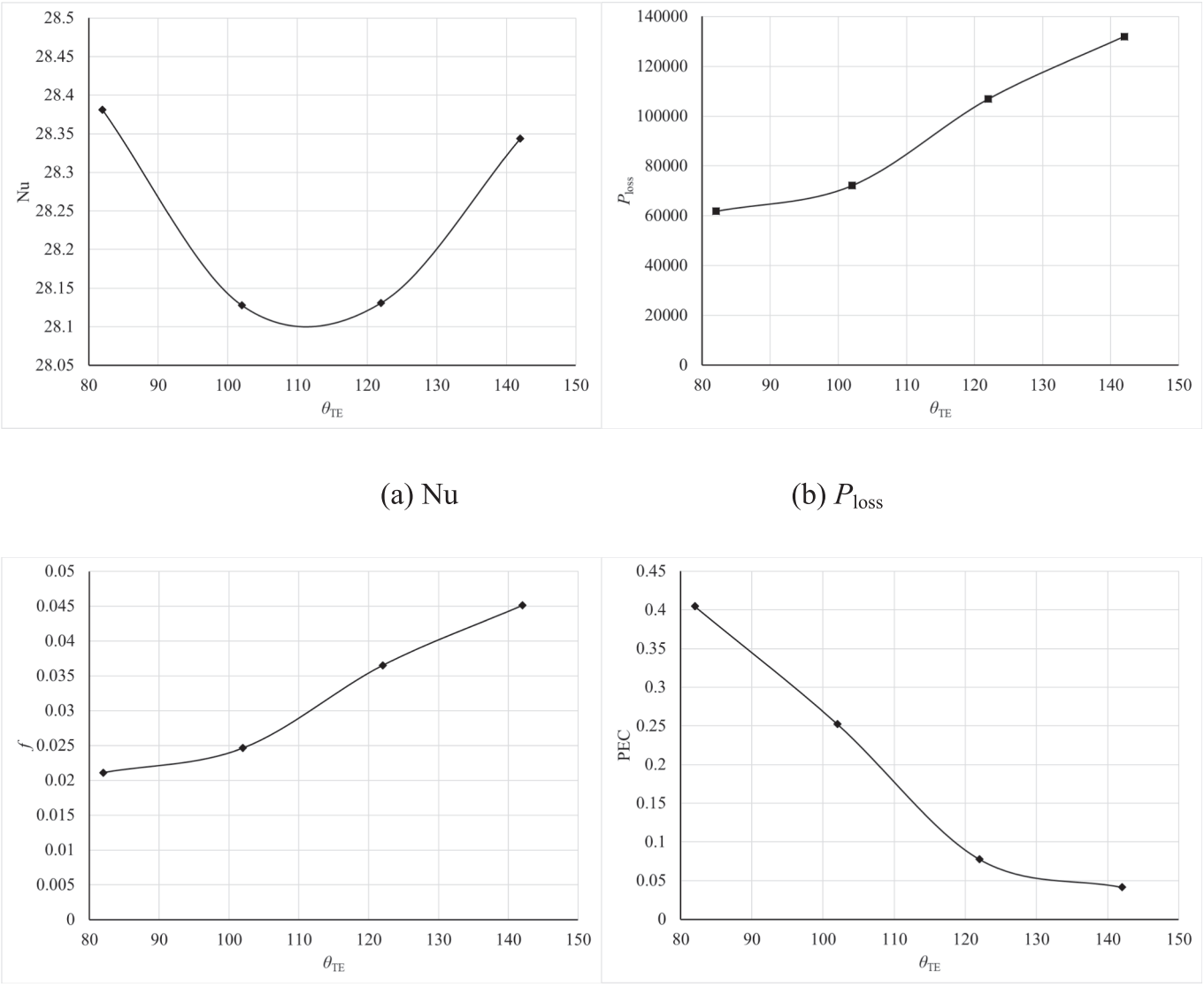

Fig. 16. Key performances with different θ_{TE} angles.

tube from 1 m < Z < 6 m. In order to more easily distinguish the effects of different wrap angles θ_{TE} on the Nusselt number *Nu*, two ranges (0 m < Z < 1 m and 2 m < Z < 3 m) were selected. From Fig. 17 (b) and Fig. 17 (c), it can be observed that the *Nu* distribution curve on Line 2 of the case $\theta_{TE} = 142°$ is higher than in the other three cases, since the increase of θ_{TE} causes a grow of the swirl intensity in the tube. The swirl plays a major role in enhancing the heat transfer. The *Nu* curves of the case $\theta_{TE} = 102°$ and the case $\theta_{TE} = 122°$ get closer from 0.4 m < Z < 6 m. The *Nu* distribution curve on Line 2 for case $\theta_{TE} = 82°$ is slightly lower than that for case $\theta_{TE} = 142°$.

3.2. *Effects on heat transfer characteristics for different blade numbers*

Fig. 18 shows the velocity streamline behind the guide vane for different blade number N. As N increases, the flow velocity in the tube is faster, and this suggests that the convective heat transfer can be enhanced by guide vanes. The main reason for the increase in flow velocity is the increase of blade number, the flow area of the blade to blade decreases. When N = 3 and N = 4, it is observed that the streamlines between the blade to blade are tangled. It means that the 3 blades or 4 blades are not enough to effectively control the secondary flow, which

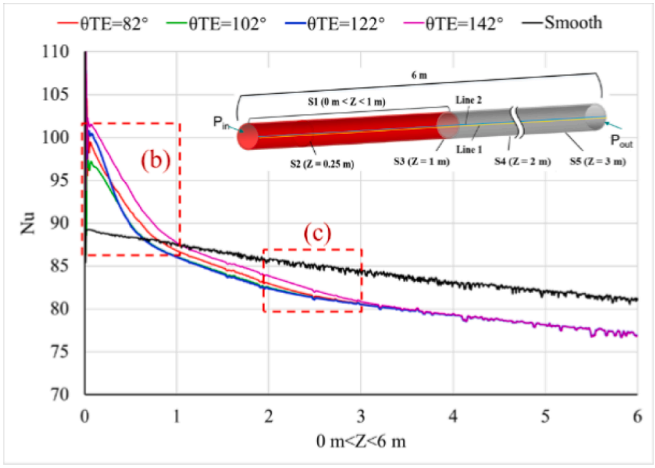

(a) 0 m< Z <6 m

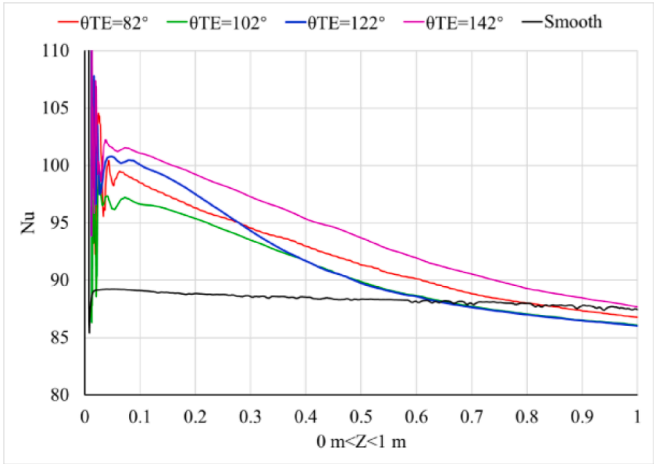

(b) 0 m< Z <1 m

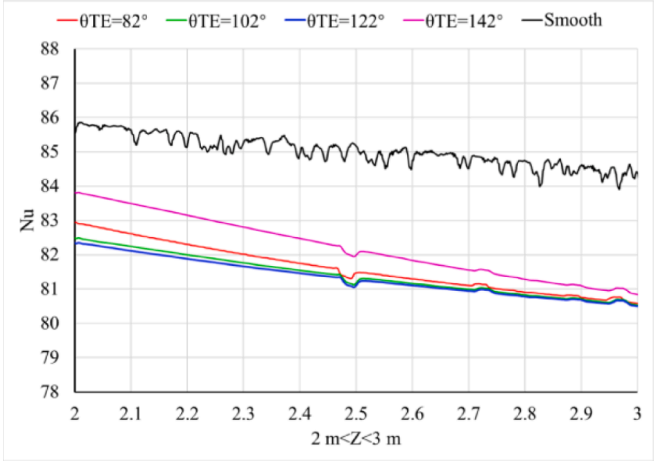

(c) 2 m< Z <3 m

Fig. 17. Nu distributions on Line 2 for different θ_{TE}.

will consume more energy, reduce swirl. When N = 5, the flow separation within the vanes slightly improves. When N ≥ 6, the flow separation in the guide vanes is well controlled.

In order to further explain the influence of different different blade number N on the inner flow in the target tube, we select the velocity swirling strength inside the guide vane and target tube to compare the differences of the different schemes, as show in Fig. 19. Analogously to Fig. 11, we only select the length range near 0–1000 mm for comparison, and the length of the lower boundary of the velocity swirling strength scale 100–200 s^{-1} to evaluate the swirling strength and the ability to enhance heat transfer. It can be observed that, the lower boundary 100 s^{-1} almost increases with the blade number N, as shown by the black dotted line. The length of N = 6, 7, 8 are much higher than 1000 mm, the length of N = 3, 4, 5 is lower than 1000 mm. The length of N = 8 is the highest.

In order to further investigate the influence mechanism of the blade number on the swirling, we select the swirling strength distribution within 0–200 mm, as shown in Fig. 20. We mark the peaks of some contours, as shown by the two black dot lines. It can be observed that the distribution of swirling strength increases gradually when the number of blades increases.

Fig. 21 shows the temperature contours on the outer surface S1 of the receiver tube for different blade numbers. In order to distinguish the effects of different blade numbers on the temperature uniformity, the preset tube, guide vane, and target tube with 0 m < Z < 1 m were selected. As the number of blades increases, the temperature on S1 gradually decreases, and the temperature peak on S1 gradually extends to the outlet direction. This indicates that by increasing the number of blades, the heat transfer is enhanced and temperature uniformity improves.

Fig. 22 shows temperature distributions on Line 1 for different blade number N. Fig. 22 (a) shows temperature distributions on Line 1 from 0 m < Z < 6 m. For the tube with guide vanes, the temperature on Line 1 for different blade numbers decrease rapidly at the beginning along the axial direction, mainly because the guide vane swirling has a great effect on enhancing heat transfer. With the weakening of the swirling flow in the tube, the heat transfer effect gradually decreases, and the temperature on Line 1 of different blade numbers increase. After Z = 3 m, the temperature on Line 1 of different blade numbers varies slightly. The overall temperature distribution on Line 1 of each case is about 50 K lower than that for the smooth tube, which effectively improves the thermal stress caused by the high temperature gradient on the tube wall. In order to better evaluate the effects of different blade number on the temperature, two Z ranges are considered (0 m < Z < 1 m and 2 m < Z < 3 m), as shown in Fig. 22 (b) and Fig. 22(c).

In Fig. 22 (b), for different blade numbers, the temperature distributions are similar. Moreover, the temperature distribution curve decreases when the blade number increases. Along the axial direction, the temperature distribution curves can be divided into two groups: one with number of blades N = 3, 4, 5, and the other with N = 6, 7, 8. The temperature for N = 6, 7, 8 are lower than N = 3, 4, 5, as shown in Fig. 22 (b) and Fig. 22 (c). For reducing the temperature peak on Line 1, it is better to choose N = 6,7,8. This temperature peak reduction will lower the thermal stress on the wall.

Fig. 23. shows the temperature difference between Line 1 and H_{min} Line for different blade numbers. The temperature curves of all cases increase rapidly along axial direction 0 m < Z < 3.5 m. From The temperature curves in Fig. 23(a) are divided into two groups along axial direction 0 m < Z < 3.5 m. These were mentioned above and have N = 3, 4, 5 and N = 6, 7, 8. The temperature for N = 3, 4, 5 are higher than N = 6, 7, 8, as shown in Fig. 23(b). The group N = 6,7,8 represents the best choice for improving the temperature uniformity of the tube wall.

Table 4 shows key performances with different blade numbers. The key performances include the Nusselt number *Nu*, the pressure drop P_{loss}, the friction factor *f*, the performance evaluation criterion (PEC), which are defined in Equation (7)–(12). According to the data in the Table 4, the variation laws of four key performances (Nusselt number *Nu*, Pressure loss P_{loss}, friction factor *f* and PEC) with blade number are analyzed respectively, as shown in Fig. 24. From Fig. 24(a), it can be observed that *Nu* increases when the blade number increases. But *Nu* with N = 6,7,8 does not change significantly. For enhancing the heat

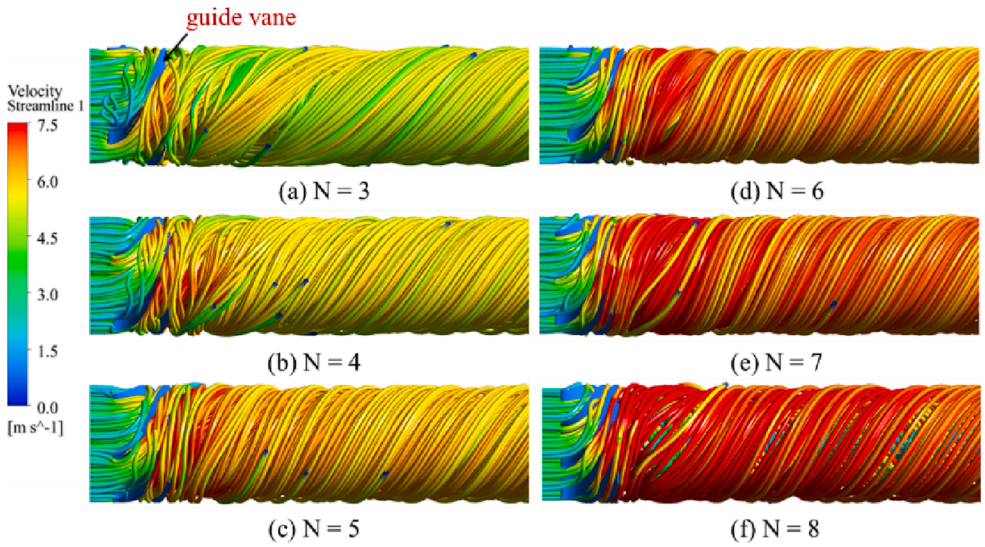

Fig. 18. Velocity streamline behind the guide vane at different blade number.

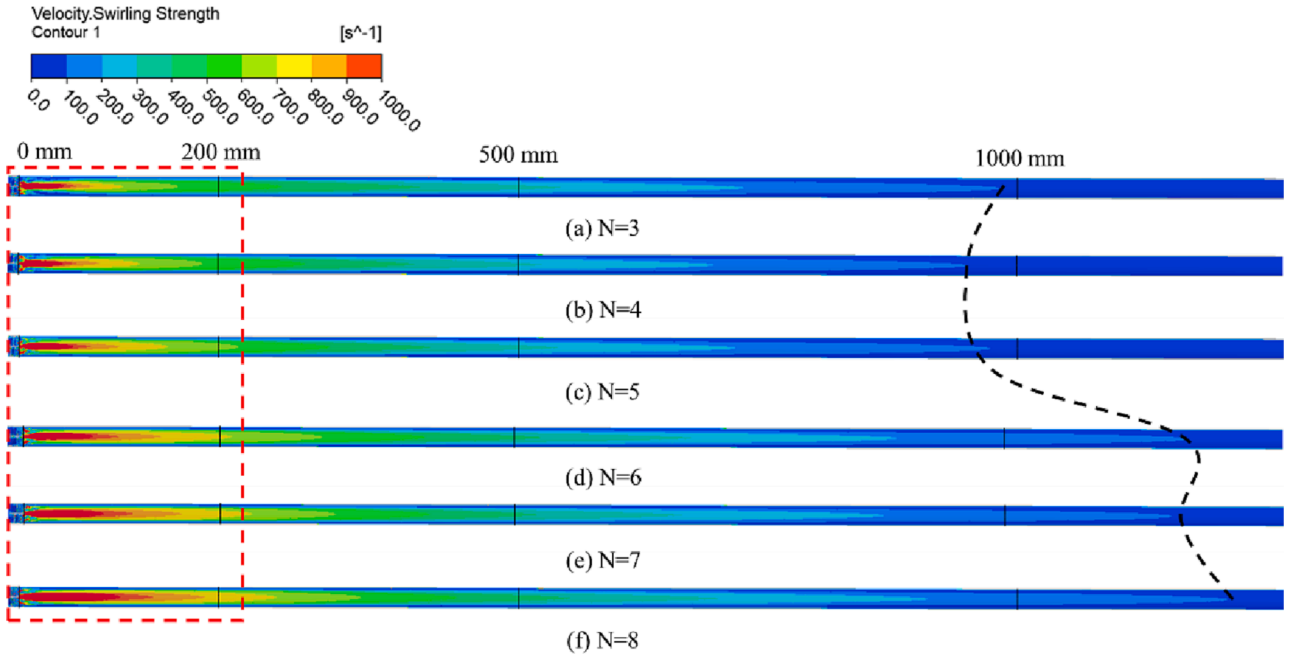

Fig. 19. Velocity swirling strength distribution for different blade number.

transfer, group N = 6, 7, 8 should be selected. From Fig. 24(b), it can be observed that P_{loss} increases when the blade number N increases. It can be concluded that, by increasing the blade number, the convection heat transfer can be enhanced, but the pressure loss will increase. Fig. 24(d) shows that the values of PEC decrease gradually with the grow of the blade number. It is also observed, that the values of PEC of all cases are lower than 1.0, which means that the thermo-hydraulic performance is poor [4]. When considering the enhancing the heat transfer, the improving the temperature non-uniformity and the flow resistance in the tube, the most convenient blade number is N = 6.

Fig. 25(a) shows the Nu distributions on Line 2 for different blade numbers. Fig. 21(a) shows the *Nu* distributions on Line 2 from 0 m < Z < 6 m. Compared with the smooth tube [26], it is evident that after adding the guide vane, the *Nu* distributions on Line 2 are larger than those of the smooth tube at the beginning (0 < Z < 1), mainly because the guide vane swirling has a great effect on enhancing the heat transfer. However, the *Nu* distributions on Line 2 become lower than those of the smooth tube from 1 < Z < 6. In order to better understand the effects of different blade numbers on the Nusselt number *Nu*, two Z ranges (0 m < Z < 1 m and 2 m < Z < 3 m) were selected. Fig. 25(b) and Fig. 21 (c) show that the *Nu* distributions on Line 2 for N = 8 are higher than those in the other cases, because when the blade number increases the swirl intensity in the tube increases. The swirl plays a major role in enhancing the heat transfer. The *Nu* distributions curves on Line 2 for group N = 6,7,8 are very closer. It is evident, that the *Nu* distribution curves are divided into two groups along axial direction 0 m < Z < 3 m. These correspond to N = 3, 4, 5 and N = 6, 7, 8.

The curves for N = 3, 4, 5 are lower than those corresponding to N = 6, 7, 8, as shown in Fig. 25(b) and (c). For enhancing the heat transfer, the best group is N = 6,7,8.

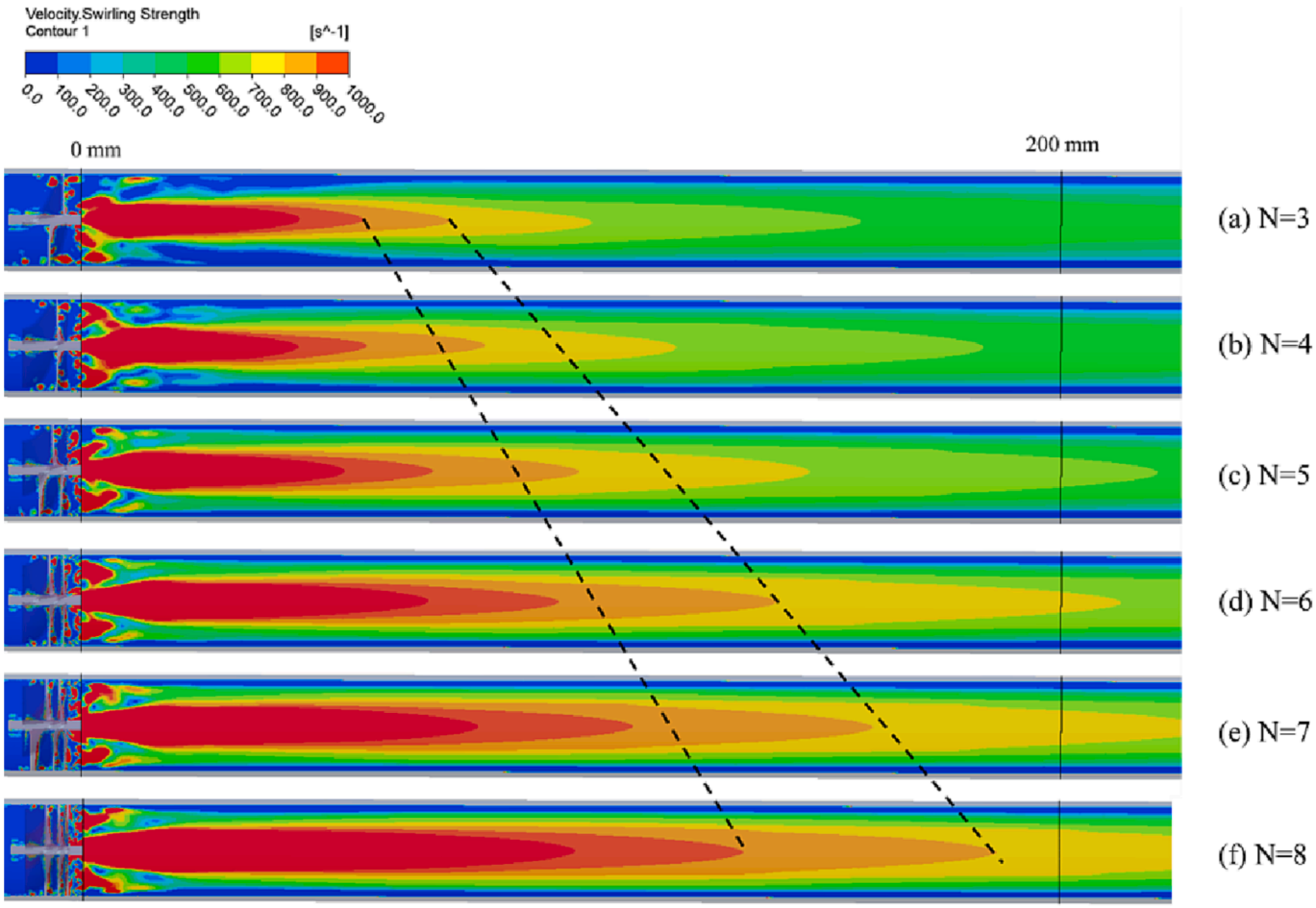

Fig. 20. Velocity swirling strength distribution (from 0 to 200 mm) for different blade number.

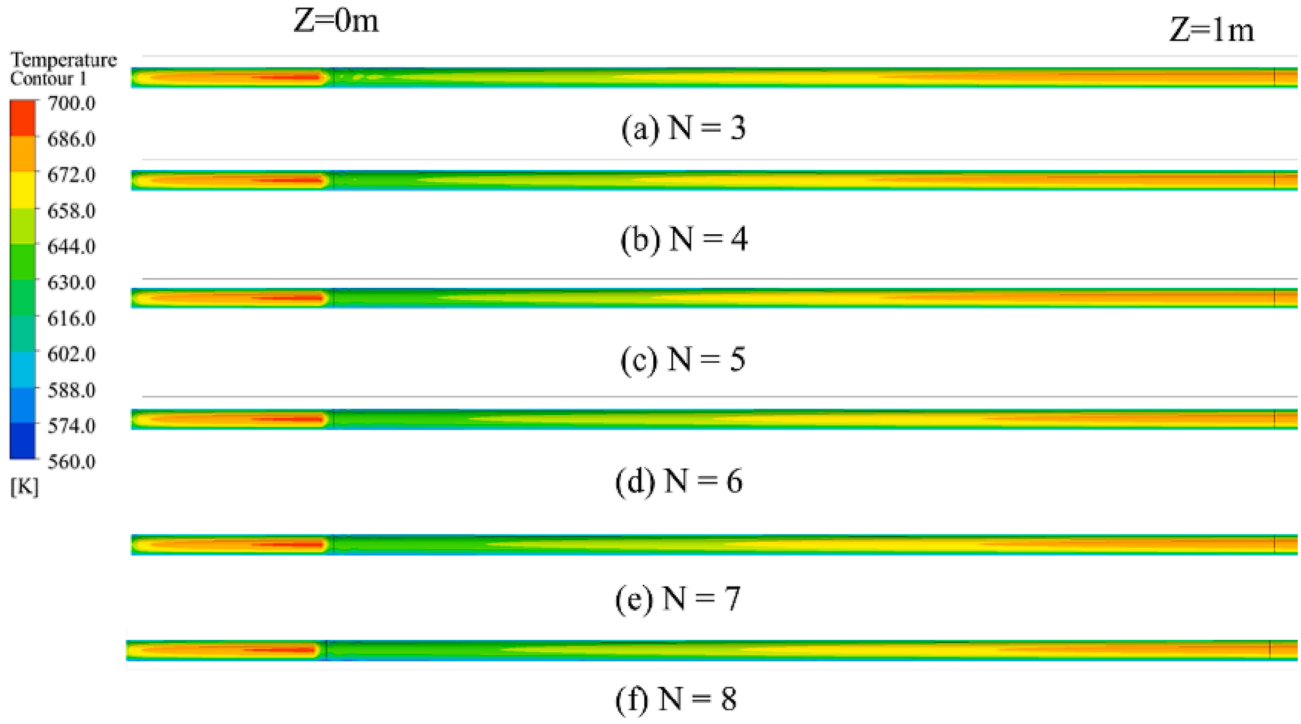

Fig. 21. Temperature contours on S1 for different blade number.

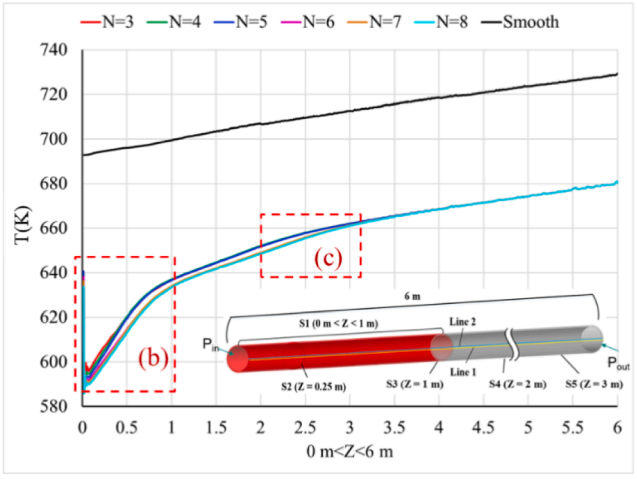

(a) 0 m< Z <6 m

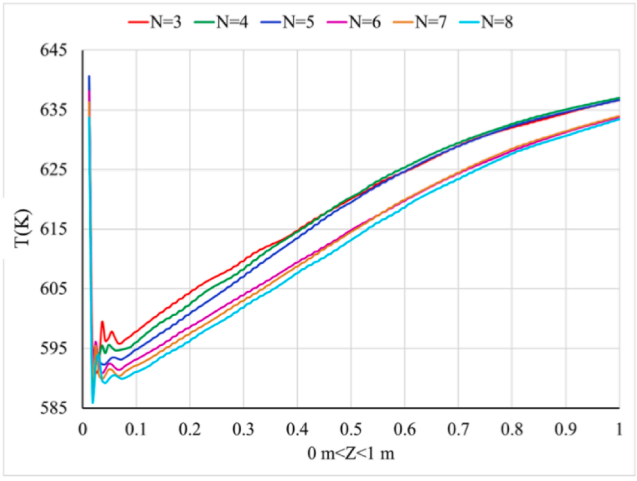

(b) 0 m< Z <1 m

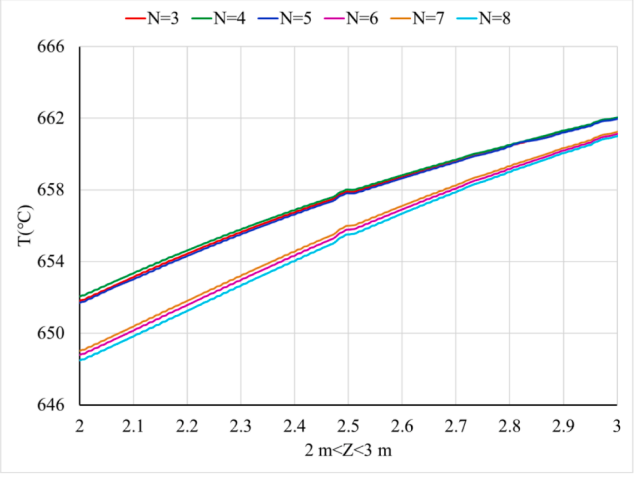

(c) 2 m< Z <3 m

Fig. 22. Temperature distributions on Line 1 for different blade number.

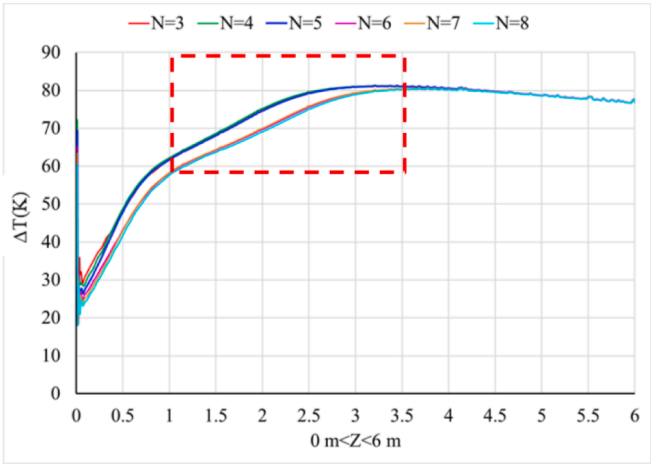

(a) 0 m< Z <6 m

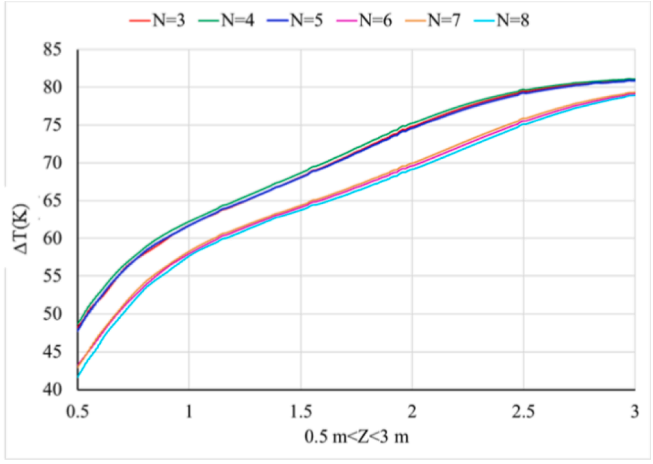

(b) 0.5 m< Z <3 m

Fig. 23. Temperature difference between Line 1 and H_{min} Line for different blade number.

4. Conclusion

In this paper, the heat transfer performances of external receiver tubes with novel guide vane components were numerically studied. The optimization of novel guide vanes could enhance the heat transfer inside the tube and improve the non-uniformity of temperature distribution on the tube surface. These numerical studies were carried out under a non-uniform heat flux distribution. Firstly, the numerical models of tube with different guide vanes (different wrap angle at trailing angle and blade number) were created. The numerical calculation of each case was carried out by using the fine meshing method and high-precision algorithm. The temperatures, pressure loss, velocity, swirling and Nusselt numbers predicted by these models were analyzed and compared. Finally, the effects of different geometric parameters on the heat transfer enhancement and on the improvement of the temperature distribution uniformity were studied.

Higher circumferential velocity means that the fluid will obtain greater swirling strength after flowing out of the guide vane, resulting in greater heat transfer capacity. When $\theta_{TE} = 142°$, the velocity swirling strength is higher. The case $\theta_{TE} = 142°$ have a first impact on the temperature on Line 1. The case $\theta_{TE} = 82°$ have a second impact on the temperature of Line 1. Through analysis the Nusselt number *Nu*, it is found the case $\theta_{TE} = 82°$and the case $\theta_{TE} = 142°$ can better enhance the

Table 4
Key performances with different blade number.

N	Nu	P_{loss}	f	Nu_c	P_{lossc}	f_c	PEC
3	28.215	82552.6	0.02822	29.308	46373.1	0.01579	0.16868
4	28.216	92784.4	0.03172	29.308	46373.1	0.01579	0.11881
5	28.232	101,685	0.03476	29.308	46373.1	0.01579	0.09031
6	28.319	111,513	0.03812	29.308	46373.1	0.01579	0.06869
7	28.321	120,985	0.04136	29.308	46373.1	0.01579	0.05379
8	28.344	131,964	0.04512	29.308	46373.1	0.01579	0.04148

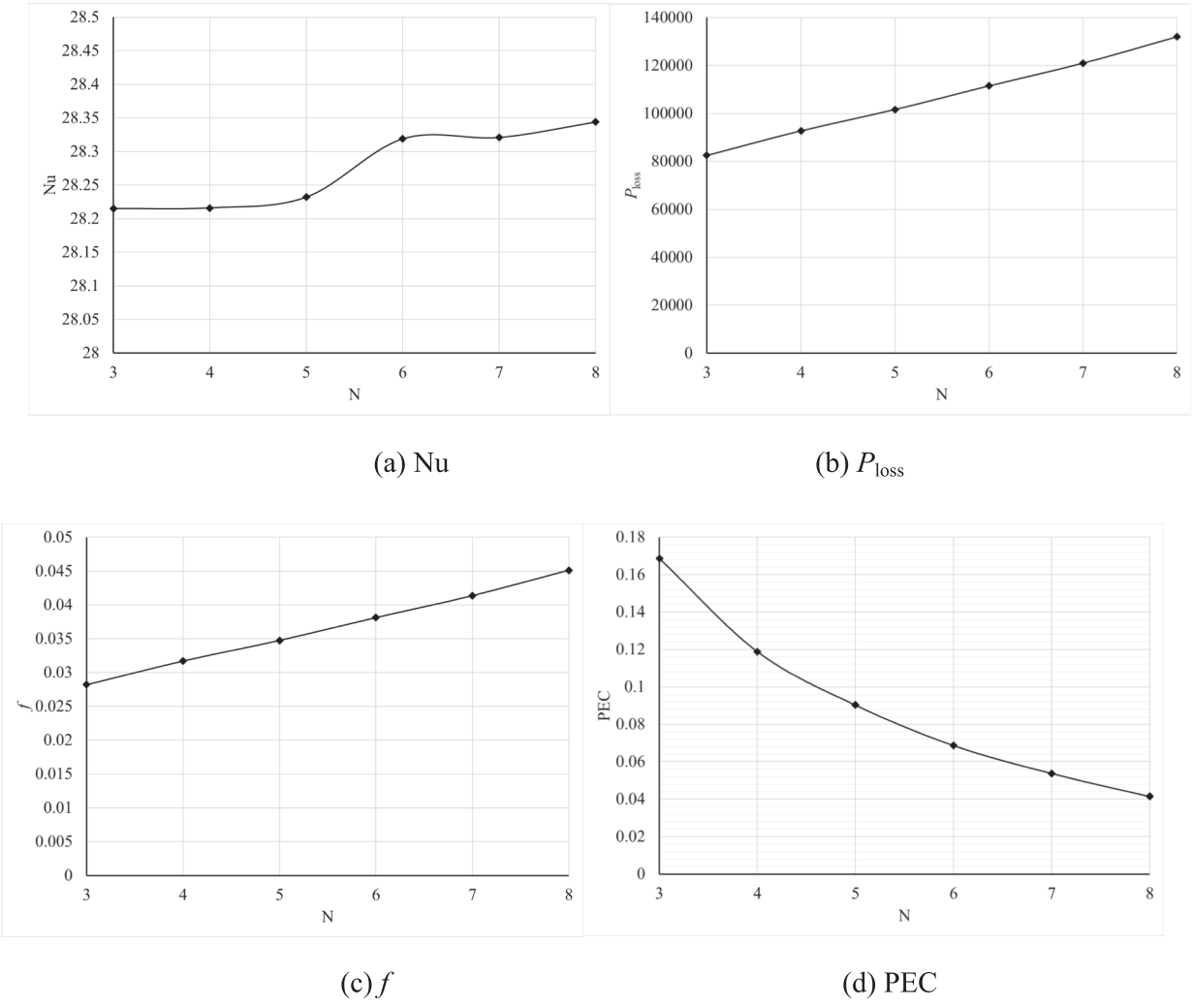

Fig. 24. Key performances for different blade number.

convection heat transfer. However, P_{loss} increases when θ_{TE} increases, and PEC decreases when θ_{TE} grows. The *Nu* distribution curve on Line 2 for $\theta_{TE} = 142^\circ$ is higher than that for the other three cases, and for $\theta_{TE} = 82^\circ$ is slightly lower than that for $\theta_{TE} = 142^\circ$. For enhancing the heat transfer, and for improving the temperature uniformity and the flow resistance in the tube, a value of $\theta_{TE} = 82^\circ$ is should be chosen.

With the increase of the blade number, the flow separation will be better controlled, and the swirling strength will increase gradually. To increase the number of blades helps to enhance the heat transfer and improve the temperature uniformity. For reducing the temperature peak on Line 1 and to improve the temperature uniformity on tube surface, a blade number N in (6,7,8) should be considered since it reduces the thermal stress on the wall when high heat flux densities are involved. The PEC decreases gradually when the blade number increases. A higher blade number will increase the system resistance and affect the thermal hydraulic performance, and also increase the design head and power of the pump. The most convenient blade number is N = 6.

The guide vane is very effective in enhancing the heat transfer inside the tube and improving the temperature uniformity on the tube surface. By optimizing the design of the two parameters, wrap angle and number of blades, better heat transfer performance and improved uniformity can be obtained.

The research in this paper will help improve the heat transfer efficiency of solar heat exchanger tubes, the energy-saving design of the new structure of heat exchanger tubes, and solve the problem of structural fatigue caused by ununiform heating of heat exchanger tubes. This study will provide theoretical basis and technical support for the efficient and reliable operation of solar collector heat exchanger tubes.

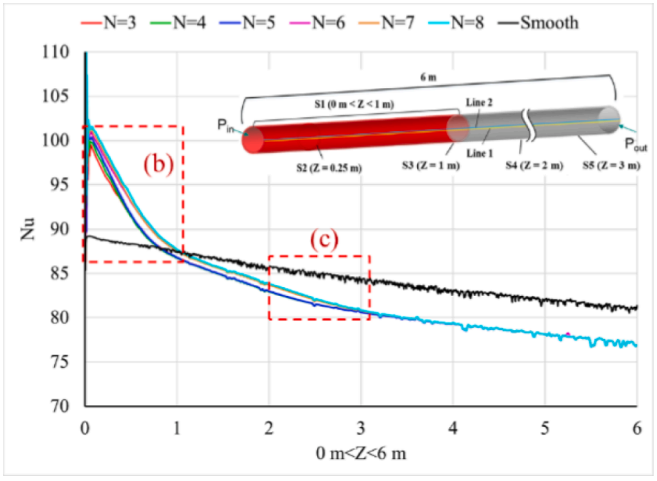

(a) 0 m< Z <6 m

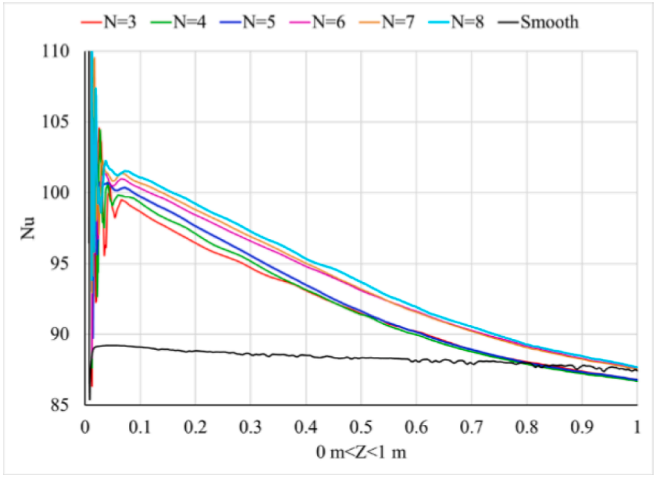

(b) 0 m< Z <1 m

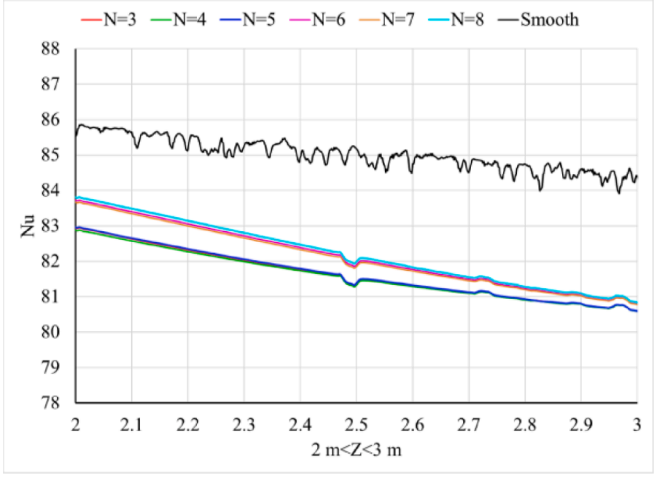

(c) 2 m< Z <3 m

Fig. 25. *Nu* distributions on Line 2 for different blade numbers.

Declaration of Competing Interest

The authors declare that they have no known competing financial interests or personal relationships that could have appeared to influence the work reported in this paper.

Data availability

Data will be made available on request.

Acknowledgments

The authors acknowledge support by the state of Baden-Württemberg through bwHPC. This work was financially supported by the China and Germany International Postdoctoral Exchange Fellowship Program by the Office of China Postdoctoral Council and the Helmholtz Centre (grant No: 20191030 , grant No: 2020030), the National Natural Science Foundation of China (grant No: 51906105, grant No: 51906085, No. U20A20292). This work was also funded by the China Postdoctoral Science Foundation Funded Project (grant No.2019 M651734, 2023 M733355), Jiangsu Province Innovation and Entrepreneurship Doctor Project (2019), Zhejiang Postdoctoral Project (2019).

References

[1] W. Ding, T. Bauer, Progress in Research and Development of Molten Chloride Salt Technology for Next Generation Concentrated Solar Power Plants, Engineering (2021).
[2] Y.L. He, K. Wang, Y. Qiu, et al., Review of the solar flux distribution in concentrated solar power: non-uniform features, challenges and solutions, Appl. Therm. Eng. 149 (2019) 448–474.
[3] J.E. Pacheco, Final test and evaluation results from the Solar Two Project, Sandia National Laboratories (2002).
[4] Z.-J. Zheng, M.-J. Li, Y.-L. He, Thermal analysis of solar central receiver tube with porous inserts and non-uniform heat flux, Appl. Energy 185 (2017) 1152–1161.
[5] SolarPACES. CSP projects around the world. Available from <https://www.solarpaces.org/csp-technologies/csp-projects-around-the-world/>, 2020 [Last accessed on 17 April 2020].
[6] O. Farges, J.J. Bezian, H. Bru, et al., Life-time integration using Monte Carlo Methods when optimizing the design of concentrated solar power plants, Sol. Energy 113 (2015) 57–62.
[7] A. Sanchez-Gonzalez, D. Santana, Solar flux distribution on central receivers: A projection method from analytic function, Renew. Energy 74 (2015) 576–587.
[8] H.E. Reilly, G.J. Kolb, An evaluation of molten-salt power towers including results of the solar two project, Sandia National Laboratories (2001).
[9] C.M. Kramer, Z.A. Munir, J.V. Volponi, Screening test of sodium nitrite decomposition, Solar Energy Materials 6 (1981) 85–95.
[10] H. Benoit, L. Spreafico, D. Gauthier, et al., Review of heat transfer fluids in tube-receivers used in concentrating solar thermal systems: properties and heat transfer coefficients, Renew. Sustain. Energy Rev. 55 (2016) 298–315.
[11] J. Fang, C. Zhang, N. Tu, et al., Thermal characteristics and thermal stress analysis of a superheated water/steam solar cavity receiver under non-uniform concentrated solar irradiation, Appl. Therm. Eng. 183 (2) (2021), 116234.
[12] L. Borghero, M. Bressan, D. Ferrero, M. Santarelli, D. Papurello, Methane-Assisted Iron Oxides Chemical Looping in a Solar Concentrator: A Real Case Study, Catalysts 12 (11) (2022) 1477, https://doi.org/10.3390/catal12111477.
[13] C. Liu, M. Du, R. Zhou, et al., Experimental investigation on thermal characteristics of a novel mesh flat-plate heat receiver in a solar power tower system, Energy 242 (2022).
[14] J.M. Lata, M. Rodriguez, M.A. Lara, High flux central receivers of molten salts for the new generation of commercial stand-alone solar power plants, J. Sol. Energy Eng. 130 (2008), 021002.
[15] Y. Qiu, Y.L. He, P.W. Li, et al., A comprehensive model for analysis of real-time optical performance of a solar power tower with a multi-tube cavity receiver, Appl. Energy 185 (2017) 589–603.
[16] B.C. Du, Y. Qiu, Y.L. He, et al., Study on heat transfer and stress characteristics of the pressurized volumetric receiver in solar power tower system, Appl. Therm. Eng. 133 (2018) 341–350.
[17] S.M. Besarati, D. Yogi Goswami, E.K. Stefanakos, Optimal heliostat aiming strategy for uniform distribution of heat flux on the receiver of a solar power tower plant, Energ. Conver. Manage. 84 (2014) 234–243.
[18] A. Sanchez-Gonzalez, M.R. Rodriguez- Sanchez, D. Santana, Aiming strategy model based on allowable flux densities for molten salt central receivers, Sol. Energy 157 (2017) 1130–1144.
[19] R. Gee, R. Winston, A Non-Imaging Secondary Reflector for Parabolic Trough Concentrators, Duke Solar Energy, Raleigh, NC, 2001.
[20] K. Wang, Y.L. He, Z.D. Cheng, A design method and numerical study for a new type parabolic trough solar collector with uniform solar flux distribution, Science China – Technological Sciences 57 (2014) 531–540.
[21] O.A. Akbari, H.H. Afrouzi, A. Marzban, et al., Investigation of volume fraction of nanoparticles effect and aspect ratio of the twisted tape in the tube, J. Therm. Anal. Calorim. 129 (2017) 1911–1922.
[22] S. Eiamsa-ard, C. Thianpong, P. Eiamsa-ard, et al., Thermal characteristics in a heat exchanger tube fitted with dual twisted tape elements in tandem, Int. Commun. Heat Mass Transfer 37 (2010) 39–46.

[23] J. Munoz, A. Abanades, Analysis of internal helically finned tubes for parabolic trough design by CFD tools, Appl. Energy 88 (2011) 4139–4149.
[24] Z.D. Cheng, Y.L. He, F.Q. Cui, Numerical study of heat transfer enhancement by unilateral longitudinal vortex generators inside parabolic trough solar receivers, Int. J. Heat Mass Transf. 55 (2012) 5631–5641.
[25] M. Borunda, R. Garduno-Ramirez, O.A. Jaramillo, Optimal operation of a parabolic solar collector with twisted-tape insert by multi-objective genetic algorithms, Renew. Energy 143 (2019) 540–550.
[26] Z. Tu, D. Piccioni Koch, N. Sarunac, et al., Thermal Analysis of a Solar External Receiver Tube with a Novel Component of Guide Vanes, Energies 14 (8) (2021) 2253.
[27] M.A. Khuda, J. Khalesi, Z. Tu, et al., Numerical analysis of a developing turbulent flow and conjugate heat transfer for molten salt and liquid sodium in a solar receiver, Appl. Therm. Eng. 217 (2022), 119156.
[28] J.J. Li, Y.L. Qian, J.L. Yin, H. Li, W. Liu, D.Z. Wang, Large eddy simulation of unsteady flow in gas–liquid separator applied in thorium molten salt reactor, Nucl. Sci. Tech. 29 (5) (2018) 62.
[29] J. Yin, Y. Qian, T. Zhang, et al., Measurement on the flow structure of a gas-liquid separator applied in TMSR, Ann. Nucl. Energy 126 (2019) 20–32.
[30] J. Yin, Y. Qian, Y. Ma, et al., Numerical and experimental study on an isolated bubble in the swirling separator, Nucl. Eng. Des. 350 (2019) 107–115.
[31] ANSYS Inc., ANSYS FLUENT Theory's Guide, Release 2020 R1, USA, 2020.
[32] https://www.scc.kit.edu/dienste/bwUniCluster_2.0.php.
[33] M.Z. Chen, Fundamentals of Viscous Fluid Dynamics, High Education Press, Beijing, 2002.
[34] A. Fritsch, R. Uhlig, L. Marocco, et al. A comparison between transient CFD and FEM simulations of solar central receiver tubs using molten salt and liquid metals. Solar Energy, 155 (2017) 259- 266.
[35] Y.L. He, W.Q. Tao, Convective heat transfer enhancement: mechanism, techniques and performance evaluation, Adv. Heat Transfer 46 (2014) 87–186.